Dynamic Effects in Capillary Pressure Relationships for Two-Phase Flow in Porous Media: Experiments and Numerical Analyses

Diganta Bhusan Das
Dept. of Chemical Engineering, Loughborough University, Loughborough LE11 3TU, U.K.

Mahsanam Mirzaei
Dept. of Engineering Science, The University of Oxford, Oxford OX1 3PJ, U.K.

Well defined experiments and numerical analyses are conducted to determine the importance of dynamic effect in capillary pressure relationships for two-phase flow in porous media. Dynamic and quasi-static capillary pressure-saturation (P^c-S_w) and, $\partial S_w/\partial t$-t curves are determined. These are then used to determine the dynamic effects, indicated by a dynamic coefficient (τ) in the porous domains which establishes the speed at which flow equilibrium ($\partial S_w/\partial t = 0$) is reached. τ is found to be a nonlinear function of saturation which also depends on the medium permeability. Locally determined τ seems to increase as the distance of the measurement point from the fluid inlet into the domain increases. However, the functional dependence τ-S_w follows similar trends at different locations within the domain. We argue that saturation weighted average of local τ-S_w curves can be defined as an effective τ-S_w curve for the whole domain which follows an exponential trend too. © 2012 The Authors. AIChE Journal, published by Wiley on behalf of the AIChE. This is an open access article under the terms of the Creative Commons Attribution License, which permits use, distribution and reproduction in any medium, provided the original work is properly cited. AIChE J, 58: 3891–3903, 2012
Keywords: two-phase flow, porous media, transient flow, quasi-static flow, capillary pressure, saturation, dynamic effect

Introduction

To characterize a variety of industrial problems (e.g., remediation of contaminated subsurface), one needs to quantify two-phase flow in porous media. Various authors have developed numerical schemes to quantify such flow behavior in which the relationships between capillary pressure (P^c) and water saturation (S_w) are needed. The P^c-S_w relationships are largely determined by well defined experiments in the laboratories using porous samples of 10–12 cm height. In these experiments, P^c is calculated by measuring the difference in average nonwetting (P_{nw}) and wetting (P_w) fluid phase pressures, expressed as a function of wetting phase saturation (S_w)

$$P_{nw} - P_w = P^{c,equ}(S_w) = f(S_w) \tag{1}$$

In Eq. 1, $P^{c,equ}$ is the capillary pressures at equilibrium saturation condition ($\partial S_w/\partial t = 0$). Traditionally, the capillary pressure relationship in Eq. 1 is defined to include a combined effect of all the factors that influence the equilibrium saturation distribution in the porous sample, namely, fluid properties (e.g., surface tension, viscosity, and density ratios), medium properties (e.g., pore size distribution, permeability and poros-

ity) and so on. However, the determination of the equilibrium P^c-S_w relationships is a time consuming process and the fluids do not necessarily flow under the equilibrium condition, particularly at smaller time durations when S_w changes with time is fast implying that the time derivative of saturation ($\partial S_w/\partial t$) may be high. Under these circumstances, P^c-S_w relationships strongly depend on both S_w and $\partial S_w/\partial t$. This dependence is known as the dynamic effect.[1–4] There are a number of authors who suggest that the conventional quasi-steady capillary pressure relationship as given in Eq. 1 may not describe the two-phase flow behavior under the dynamic conditions.[1–19] It was suggested that Eq. 1 should be generalized to include a capillary damping or dynamic coefficient (τ) as below[6]

$$\left(P^{c,dyn} - P^{c,equ}\right)\big|_{S_w} = -\tau(\partial S_w/\partial t)\big|_{S_w} \tag{2}$$

where, $P^{c,dyn} = P_{nw}^{dyn} - P_w^{dyn}$ and $P^{c,equ}$ are the capillary pressures at dynamic and equilibrium conditions, all measured at the same S_w. As evident, the equation has the general form of a straight line and, in theory, should pass through the origin on a plot of $\left(P^{c,dyn} - P^{c,equ}\right)$ vs. $\partial S_w/\partial t$. The slope of this linear relationship is the dynamic coefficient (τ). These are discussed in detail by Mirzaei and Das[2] and Das et al.[3] and the references therein where the values of t are reported to range from 1.93×10^6 to 9.95×10^9 Pa s. Recently, more studies on determination of τ and its physical interpretation have been reported[4,18–20] which suggest the importance of obtaining the values of the dynamic coefficient. Other recent work[21,22] in the area have focused on developing numerical codes for
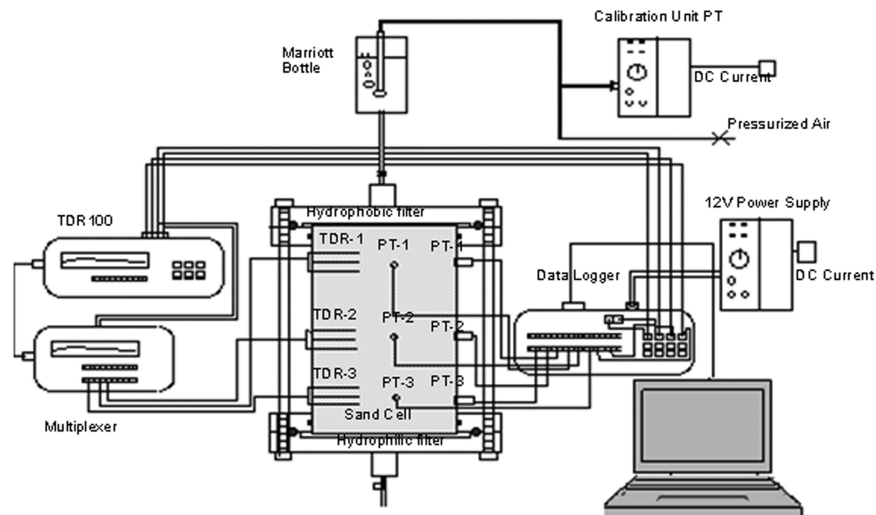
Figure 1. Sketch of experimental set up.

simulating two-phase flow in porous media based on the dynamic capillary pressure relationship (Eq. 2).

Despite the knowledge that has accumulated so far, there is still ambiguity concerning the magnitude of the dynamic coefficient and consequently dynamic P^c-S_w relationships for quantifying the dynamic two-phase flow behavior in porous media. In this regard, a number of fundamental questions need to be addressed carefully, e.g., can the functional dependence of the dynamic coefficient on porous medium properties such as the permeability be measured experimentally and the interpretation of these relationships. This article aims to resolve these issues through well-defined laboratory experiments. In particular, the experimental characterization of dynamic coefficient in two different types of porous media is attempted. The experimental results of silicone oil-water flow in homogeneous porous domains are presented to explore the effect of porous medium properties by considering samples with different grain size, e.g., bulk permeability, porosity and pore size distribution index.

To achieve the aims of this article, we have designed in-house experiments for determining local and effective (average) P^c-S_w relationships for two-phase flow in homogeneous porous media. The experiments are specifically aimed at (1) understanding the behavior of P^c-S_w relationship caused by applied boundary conditions and types of porous sample and (2) quantifying dynamic effect for silicone oil-water flow in homogeneous porous media at different locations within the domain. The methodology of our experiments and, the results of drainage experiments conducted on two different porous media are presented and discussed. Transient and quasi-static experimental results are used to calculate dynamic coefficient and quantify dynamic effect locally and at the scale of the whole domain. This point is of particular interest since τ-S_w curves are determined locally and then averaged to find an effective τ-S_w curve for the full domain. The experiments are also simulated using already developed computer models[1–4] by these authors.

Materials and Experimental Methods

Experimental rig

An experimental rig (Figure 1) has been designed in this work to quantify the dynamic effect (τ) in porous media. As evident in Eq. 2, the parameters that are needed for this pur-

pose are the quasi-static ($P^{c,equ}$) and dynamic ($P^{c,dyn}$) capillary pressures, water saturation (S_w) and the time derivative of the saturation ($\partial S_w/\partial t$). Therefore, our experiments have been conducted specifically to obtain these parameters. The constructed rig involved a cylindrical cell packed with either fine or coarse-grained sand in which dynamic and steady-state flow experiments have been performed. In each experiment, silicone oil was injected at the top of a sand column (Figure 1) through a hydrophobic filter and water drained out of the cell through a hydrophilic filter at the bottom of the cell. Three mini-time domain reflectometer (mini-TDR) probes are installed at different heights in the sample to measure in situ water content during an experiment. Three pairs of pressure transducers (PTs) are also mounted on the cell wall, which are at the same heights as the mini-TDR probes. Each pair of PTs contains one PT equipped with hydrophilic filter and another with hydrophobic filter which monitor average water (P_w) and silicone oil (P_{nw}) pressures, respectively, corresponding to the S_w measurements by the TDR probe at the same height. The differences in these pressure measurements (P_{nw}-P_w) are calculated to determine local P^c at those heights. Locally measured water saturation and, capillary pressure are then used to construct the dynamic and quasi-steady P^c-S_w curves. These curves are subsequently used to calculate the dynamic coefficient (τ).

Measurement sensors

In our experiments, mini-TDR model T-3 probes (East 30 Sensors, Washington) are used for measuring water saturation in the porous sample. These are calibrated in a cell of 10.2 cm diameter and 4 cm height. For this the following procedures are adopted. The TDR probes are connected to an interface called multiplexer [synchronous device for measurement, SDMX50, Campbell Scientific (CSI), Loughborough, UK] which is then connected to a TDR unit (TDR100, CSI, Loughborough, UK) by a coaxial interconnecting cable (CSI, Loughborough, UK). The TDR100 unit is also connected to a data logger (CR10X, CSI, Loughborough, UK) to record the apparent length of the probes and a computer with a software (PCTDR, CSI, Loughborough, UK) for automatic logging of the water content.

The first step in the calibration of the mini-TDR probe is to determine the parameters of an input function of the data

Table 1. Fitting/Calibration Parameters for Determination of S_w for Our Experiments (Data Follow a Third-Order Polynomial Equation of the Form: $S_w = A + B \times K_a + C \times K_a^2 + D \times K_a^3$)

Probe Name	Probe Length (mm)	Probe Offset (mm)	A	B	C	D
TDR-1	68	5.6	−1.5996	0.3215	−0.0147	0.0002
TDR-2	65	5.7	−1.6637	0.3362	−0.0156	0.0002
TDR-3	67	5.5	−1.7824	0.3555	−0.0165	0.0003

logger program to be used to model the relevant portion of the input signal of the mini-TDR probes. For this purpose, a mini-TDR probe is connected to the TDR100 unit which is then connected to a computer running the PCTDR software. The power supply to the TDR100 unit is switched on and a waveform is collected by the PCTDR software. The collected waveforms indicate the apparent distance for waveform start and apparent waveform length for that specific probe. Waveform starts and its lengths for two other probes are also measured with the same procedure.

Having found the apparent waveform start and length values for probes, the TDR100 unit is connected to the SDM control ports of the data logger via a short five conductor cable. The cell is filled with a known amount of water and a predetermined amount of sand is then poured into the cell. Subsequently, vacuum is applied for 24 hours to take any possible trapped air out of the porous sample. The TDR100 unit is switched on and the mini-TDR probe readings are recorded with the data-logger. Next, the water-saturated sand in the cell is replaced by a sand sample which is fully saturated with oil and de-aired. Again, the data logger records the data for this sample. These two measurements provide the limiting points for calibration curve corresponding to 100% and 0% of water in the cell. Then, the sample saturated fully with a mixture of known amount of water and oil is placed in the cell. The sample is de-aired and the mini-TDR probe readings are recorded. Samples with different proportion of water and oil but the same mass are considered to find enough points for calibration curves. Knowing the exact amount of each phase in the mixture of fluid in each sample for determining various points and also the amount of single phase for the limiting points of the calibration procedure, a plot of sample water saturation vs. mini-TDR probe reading is prepared. Table 1 presents different probe lengths determined by PCTDR software and the parameters of a polynomial function calculated from curve fitting for calibrating the TDR probe. Once the calibration functions are determined for each mini-TDR probe, they are mounted in predefined locations in the cell and fixed in place by applying silicone sealant.

In this work, six PTs (XTC-190M-7 BARG, Kulite Semiconductor Products, Leonia, NJ) were used for pressure measurements. I-vyon F3.2 P4 treated (Porvair Technology, a division of Porvair Filtration Group, Wrexham, UK) polymeric filters were placed as the membrane in front of the PTs which were used to measure the pressures of the nonwetting phase (silicone oil). Vyon is naturally hydrophobic which prevents aqueous solutions from wetting out the pore structure. To make it hydrophilic, Porvair Technology applies special treatment process to enhance its surface wetting characteristics allowing immediate uptake of a wetting fluid and very high entry pressure for nonwetting fluid. To measure water pressures at three different heights of the cell, three PTs are mounted in one side of the cell. A small gap between a PT and a filter allows the fluid to accumulate in front of the PT for pressure measurement. Depending on the

wettability characteristic, each filter is de-aired and saturated with either water (wetting phase) or oil (nonwetting phase) before setting up the in situ PT calibration for pressure measurement. The de airing unit consists of two circular reservoirs to facilitate sealed installation inside the cylindrical cell for in situ de-airing and saturating. Each reservoir consists of a main flow line drilled in the middle and three holes on the side to provide connection with housing unit and main flow line. The main flow line of each reservoir is connected to inflow and outflow line at lower and upper ends to provide suction and discharge of de-airing fluids and air, respectively.

Once the de-airing and saturating is done, the flow line of vacuum pump is disconnected whilst the de-airing unit is in place. The PTs are connected to CR10X data logger for data collection. The LoggerNet 3.1 support software (CSI, Loughborough, UK) provides the facilities for communications, programming, data transfer, and data processing during calibration and through the experiment. When the calibration unit pressure is decreased to atmospheric pressure, the air pressure line is disconnected. A plot of PT reading per excitation voltage (mV/V) vs. total pressure, which is the calibration unit pressure plus hydrostatic fluid head above each PT, is plotted. It seems that a linear function gives a good fit to the data points with reasonable accuracy. Such a plot gives the calibration equation for each pair of PT. The slope of the line is multiplier and the intercept gives the offset value for each PT to program the data logger. Following the collection of calibration data, the experimental cell is carefully mounted on top of a metal plate equipped with fully saturated and de-aired hydrophilic filter. The cell is then filled with water and the de-airing unit is removed to prevent any air flow to de-aired filters and PTs. Having determined the measurement sensors calibration function to program the data logger for pressure and saturation measurements, the sample is prepared to conduct two-phase flow experiments.

Properties of porous samples and fluids

Our experiments were conducted using two commercial grades of silica sand, namely, Leighton Buzzard DA 14/25 as coarse-grained and Leighton Buzzard DA 30 as fine-grained sand (WBB Minerals, Cheshire, UK). Both sands provide high uniformity of particles ($d_{60}/d_{10} = 1.32$ for the coarse and 1.21 for the fine sand), high sphericity, high chemical purity and very low organic matter content. Silicone oil (BDH Laboratory Supplies, Poole, UK) with viscosity of 200 cSt which has negligible solubility in water, volatility at room-temperature and health risk is selected as the nonaqueous phase liquid (NAPL). The selected aqueous phase for our experiments is distilled water.

The two-phase flow experiments were carried out in a cylindrical acrylic cell, 102 mm in diameter and 120 mm in length. In all experiments, the sand was first purged of air by stirring sand in a distilled water reservoir until no air bubble came out of the mixture. The mixture was then put

Property	Coarse Sand	Fine Sand	Water	Silicon Oil
Permeability, $K(m^2)$	8.7×10^{-10}	3.1×10^{-10}	–	–
Porosity, θ(-)	0.35	0.32	–	–
Entry pressure, P^d (Nm^{-2})	510	675	–	–
Pore size distribution index, λ(-)	2.07	2.55	–	–
Residual water saturation, S_{rw}(-)	0.258	0.271	–	–
Density, ρ (kg m^{-3})	–	–	1000	968
Viscosity, μ (kg m^{-1}s^{-1})	–	–	1×10^{-3}	193×10^{-3}
Surface tension, σ (Nm^{-1})[a]	–	–	0.072[b]	0.035[c]

The media properties are determined experimentally and the fluid properties are either standard values or taken from literature.
[a]As reported in Adamson and Gast.[24]
[b]Water–air system.
[c]Silicon oil—water system.

in a vacuum unit to eliminate any trapped air bubble for 24 hours. The cell was carefully mounted on a plate equipped with an o-ring for tight sealing and, a de-aired and fully water saturated hydrophilic filter to facilitate water drainage and prevent oil flow at outflow section. Wet and de-aired sand were then poured into the cell filled with water. The whole unit is placed in a container to collect extra water and the container is placed in a mechanical shaker to provide even and dense fully water saturated packing.

The homogeneity of porous samples was checked by X-ray tomography. Once it was ascertained that the samples have homogeneous packing, the porosity of the sand pack was determined from the total mass of each sand pack. Before conducting a two-phase flow experiment, single phase flow using water and closely following constant head permeability test was performed to measure intrinsic permeability of the sand pack. To perform this experiment, a hydrophilic filter was placed on the top of the sand column and inflow reservoir (Mariotte Bottle) was filled with distilled water.

Properties of the fine and coarse sands, which include the intrinsic permeability, porosity, Brooks–Corey parameters[23] determined from quasi-static experimental results are listed in Table 2. The properties of fluids used in our experiments have also been presented in this table. The premises on which these tests take place are kept at a constant temperature of 20°C so as to avoid any influence of temperature variation on density, viscosity and surface tension of the fluids used.

Procedures for quasi-static and dynamic two-phase flow experiments

Having measured the porosity and permeability of the saturated porous sample, the upper hydrophilic filter is replaced by a hydrophobic filter and a Mariotte Bottle filled with silicone oil is connected to allow its flow into the cell (Figure 1). The Mariotte bottle provides constant pressure for the flow of oil in the experimental cell provided through a manual pressure regulator.

Quasi-static two-phase flow experiments

Our quasi-static flow experiments are conducted as follows: the outflow valve at the bottom of the cell is kept open to allow very low flow rate during experiment. It is levelled with the top of the sand to overcome hydrostatic head pressure gradient which minimizes gravity effect. The initial pressure of silicone oil is zero within sand column. However, the PTs recording the silicone oil pressure show the hydrostatic pressure head which is equal to the pressure measured by PTs measuring water pressure at the same

height. Then, the pressure of silicone oil on the top column boundary is gradually increased by increasing air pressure on top of the Mariotte bottle. This leads to infiltration of silicone oil through hydrophobic filter at the top of the cell. Injected oil displaces water out of the sand column. Water saturation (S_w) is directly measured using the three TDR probes in the experimental cell. To confirm the S_w readings, some measurements of S_w are also done considering the initial water content and outflow water volume. These are then compared with the TDR readings of average S_w. The reason why the TDR readings are used in our work to plot the P^c–S_w curves is because we are interested in the local measurements of the dynamic coefficients which will not be possible otherwise if the TDR probes are not used.

The flow experiments are carried out until steady-state flow condition is reached, i.e., the water flow rate stabilizes at outflow valve. Measured S_w and P^c provide one point of a quasi-static P^c–S_w curve. Next, the imposed air pressure on the Marriot bottle, and hence the oil pressures, is increased and the experiment is continued until a new steady state is reached. A second point for the P^c–S_w curve is thus obtained. This process is repeated several times to determine a complete P^c-S_w curve for a sample. This procedure is continued until the measured water content at the lower TDR probe reaches irreducible water content (S_{iw}) and stays constant. Then, the experimental set-up is then disassembled for cleaning and de-airing the filters for new experiments. The sample is remounted and PTs de-aired again and calibration resumed. The testing cell is reassembled and repacked with clean sand to conduct a new experiment.

Dynamic two-phase flow experiments

To conduct the dynamic two-phase flow experiments, the imposed silicone oil pressure at the top of domain is increased to a high pressure and kept constant by imposing a constant air pressure on Mariotte bottle. Table 3 shows the applied pressures for carrying out different dynamic two-phase flow experiments in this work. The dynamic two-phase flow is continued until the saturation at lower TDR probe reaches its irreducible water saturation (S_{iw}). The TDR probes measure the water content while the PTs record oil and water pressure, as explained before. They provide the necessary data to determine three local dynamic P^c-S_w curves for each boundary pressure. Once the oil front reaches the bottom filter and lower mini-TDR probe start showing the irreducible saturation (S_{iw}) the experiment is terminated. This experiment is repeated for four different conditions to provide enough dynamic P^c-S_w curves for determining τ-S_w relationships. These curves are then used with steady-state

Table 3. Boundary Conditions Applied for Different Dynamic Drainage Displacement in Cylindrical Homogeneous Porous Media Considering Pressure Cell Experiment Used for the Measurement of Two-Phase Flow Properties

		Top Boundary		Bottom Boundary	
Displacement case	Time Duration (hr)	Dirichlet Nonwetting Phase Pressure (Pa)		Dirichlet Water Pressure (Pa)	
Dynamic case-1	5.6	8	Zero Flux Water	1.2	Zero Flux
Dynamic case-2	3.9	9		1.2	Nonwetting Phase
Dynamic case-3	2.8	10		1.2	
Dynamic case-4	2.1	11		1.2	

Dirichlet boundary condition of pressure is imposed for nonwetting phase at the Top and water at the Bottom. Zero flux boundary condition is imposed for water at the Top and nonwetting phase at the bottom. This allows only nonwetting phase infiltration at the Top and water outflow at the Bottom of the pressure cell.

P^c-S_w curves to calculate the dynamic coefficient at the three different measurement heights within the column as discussed in the results.

Numerical analyses

Having conducted laboratory experiments to investigate the dynamic effect on two-phase flow in porous media, we aim to simulate these experiments in this section. The main objective is to describe the experiments using previously reported theoretical frameworks and to explore if the results from these numerical simulations compare to the experimental results. The boundary conditions (Table 3) and size of the domain for numerical simulations (Table 4) are the same as those used for laboratory experiment. Furthermore, the configuration of cylindrical domain and the governing equations (Table 5) to simulate fluid flow in porous media are the same as used by Mirzaei and Das.[2] Porous media and fluid properties are defined to be the same as those measured and/or calculated in laboratory experiment as presented in Table 2.

The procedures for simulation of dynamic and quasi-static P^c–S_w curves are described in detail by Mirzaei and Das[2] which also follow closely the experimental procedures. They are not repeated in this article due to lack of space.

Averaging methods

As explained earlier, the experimental capillary pressure–saturation (P^c-S_w) and saturation–time (S_w-t) curves are measured at three heights within the cell. Therefore, in the numerical modeling, the capillary pressure and saturation values are averaged over the three corresponding measurement volumes, namely the upper, middle and lower measurement volumes. These volumes are equal to the volumes of the porous media around each laboratory measurement points where the measurement points are located in the middle of the measurement volumes. The upper, middle and lower measurement volumes are equal.

To obtain the average P^c-S_w and S_w-t curves at the measurement heights, the capillary pressure and saturation values

of each node in the corresponding measurement volume are averaged as follows

$$(P^c|_{t_n})_{V_i} = (\langle P_{nw} \rangle|_{t_n} - \langle P_w \rangle|_{t_n})_{V_i}$$

$$= \left(\left(\frac{\sum_{j=1}^{m}(1 - S_{wj})P_{nwj}}{\sum_{j=1}^{m}(1 - S_{wj})} - \frac{\sum_{j=1}^{m}S_{wj}P_{wj}}{\sum_{j=1}^{m}S_{wj}} \right) \Bigg|_{t_n} \right)_{V_i} \quad (3)$$

where, t_n is an arbitrary nth time step, $(P^c|_{t_n})_{V_i}$ is the average capillary pressure at time t_n over a measurement volume V_i where $i = 1,2,3$ correspond to the three measurement volumes from top to bottom of the domain, $\langle P_{nw} \rangle|_{t_n}$ and $\langle P_w \rangle|_{t_n}$ are the volume averaged nonwetting and wetting phase pressure, P_{nwj} and P_{wj} are the nonwetting and wetting phase pressures and, S_{nwj} and S_{wj} are the saturations corresponding to nonwetting and wetting phase pressure at time t_n in an arbitrary jth node where $j = 1, 2, 3,… m$, m being the total number of numerical nodes in the measurement volume V_i.

At each node of the numerical grid, the saturation and volume of the wetting and nonwetting fluids are related as follows

$$V_{wj} + V_{nwj} = \phi \times V_j \quad (4)$$

$$S_\gamma = \frac{V_{\gamma j}}{V_j \times \phi}, \quad \gamma \equiv w, nw \quad (5)$$

$$S_{wj} + S_{nwj} = 1 \quad (6)$$

where, V_{wj} and V_{nwj} are the volumes of the wetting and nonwetting phases in the arbitrary node j, respectively. V_j is the volume of node j and S_{wj} and S_{nwj} are the saturation of the wetting and nonwetting phase in node j.

Average water saturation at an arbitrary time t_n in the measurement volume V_i is calculated using an averaging of saturation of individual nodes in the numerical measurement volume V_i

Table 4. Number of Nodes and Nodal Spacing for Different Domain Geometries

	Number of Nodes × Nodal Spacing in Different Geometries				
Domain Geometry	$N \times \Delta R$ (cm)	$N \times \Delta \Theta$ (°)	$N \times \Delta X$ (cm)	$N \times \Delta Y$ (cm)	$N \times \Delta Z$ (cm)
2D rectangular	–	–	8 × 1.25	1 × 7.92	1 × 0.05, 24 × 0.5, 1 × 0.05
3D rectangular	–	–	8 × 1.25	8 × 0.988	1 × 0.05, 24 × 0.5, 1 × 0.05
3D cylindrical	4 × 1.25	4 × 90	–	–	1 × 0.05, 24 × 0.5, 1 × 0.05

N, number of nodes; ΔR, nodal spacing in R direction for cylindrical domain; $\Delta \Theta$, nodal spacing in Θ direction for cylindrical domain; ΔX, nodal spacing in X direction for rectangular domains (2D or 3D); ΔY, nodal spacing in Y direction for rectangular domains (2D or 3D); ΔZ, nodal spacing in Z direction for rectangular and cylindrical domains (2D or 3D).

Table 5. Governing Equations Used in Numerical Modeling[1–4]

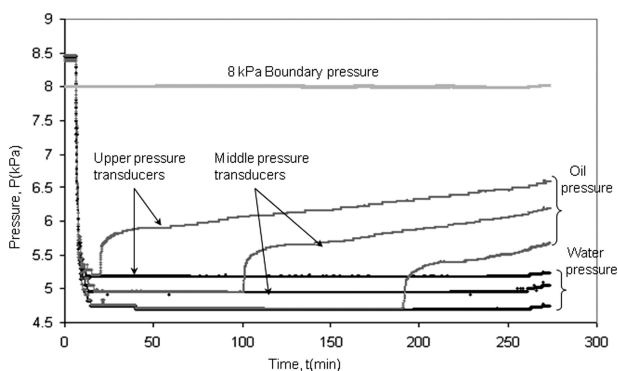| Governing Model Equations	Definition of Parameters
Extended version of Darcy's law for conservation of momentum of fluid phases $$q_\gamma + \frac{K_{r\gamma}k}{\mu_\gamma} \cdot \nabla P_\gamma = 0 \quad for \quad \gamma \equiv w, nw$$ Continuity equation for conservation of fluid saturation in porous domain $$\frac{\partial}{\partial t}(\phi \rho_\gamma S_\gamma) + \nabla \cdot (\rho_\gamma q_\gamma) = 0 \quad for \quad \gamma \equiv w, nw$$ Brooks-Corey-Burdin (Brooks-Corey, 1964) relationships for capillary pressure and relative permeability in domain $$S_{ew} = \left(\frac{P^c}{P^d}\right)^{-\lambda} \text{ for } P^c \geq P^d$$ $$S_{ew} = 1 \text{ for } P^c \leq P^d$$ $$S_{ew} = \left(\frac{S_w - S_{rw}}{1 - S_{rw}}\right), \quad 0 \leq S_{ew} \leq 1$$ $$K_{rw} = S_{ew}^{(2+\lambda)/\lambda}$$ $$K_{rnw} = (1 - S_{ew})^2 (1 - S_{ew}^{(2+\lambda)/\lambda})$$	The subscripts "w" and "nw" are the wetting (water) and nonwetting (DNAPL) fluid phases; q [LT^{-1}]: fluid flow velocity K_r [-]: relative permeability, k[L^2]: intrinsic permeability; μ [$ML^{-1}T^{-1}$]: fluid viscosity; P [$ML^{-1}T^{-2}$]: average pore pressure ϕ [-]: porosity of the medium; ρ[ML^{-3}]:fluid density; S[-] average fluid saturation in the porous medium S_{ew}[-]: effective saturation of the wetting phase; P^d [$ML^{-1}T^{-2}$]: entry pressure of the medium;λ[-]: pore size distribution index; S_{rw}[-]: irreducible wetting phase saturation

$$(S_w|_{t_n})_{V_i} = \left(\frac{\sum_{j=1}^m S_{wj}\phi_j V_j|_{t_n}}{\sum_{j=1}^m \phi_j V_j}\right)_{V_i} \quad (7)$$

Porosity of each numerical cell is the same. Hence, the porosity term in Eq. 7 can be cancelled. Based on the averaged water saturations at different times at each measurement volume, $\partial S/\partial t$ at each numerical measurement volume is then calculated. This is also the slope of average water saturation vs. time curve at any time. It is approximated based on a central differencing scheme, as shown below

$$\left(\frac{\partial S}{\partial t}|_{S_w,t_n}\right)_{V_i} = \left(\frac{S_w|_{t_{n+1}} - S_w|_{t_{n-1}}}{t_{n+1} - t_{n-1}}\right)_{V_i} \quad (8)$$

where, $S_w|_{t_{n-1}}$, $S_w|_{t_n}$, and $S_w|_{t_{n+1}}$ are the average wetting phase saturation at t_{n-1}, t_n, and t_{n+1} calculated using Eq. 7 in any numerical measurement volume.

Having determined the effective/average P^c-S_w curves and $\partial S/\partial t$ vs. time curves, Eq. 2 is applied to calculate dynamic coefficient in different numerical measurement volumes. As explained before, saturation weighted average of calculated dynamic coefficient and average wetting phase saturation values in different measurement volumes are calculated to find the average dynamic coefficient values for the whole domain.
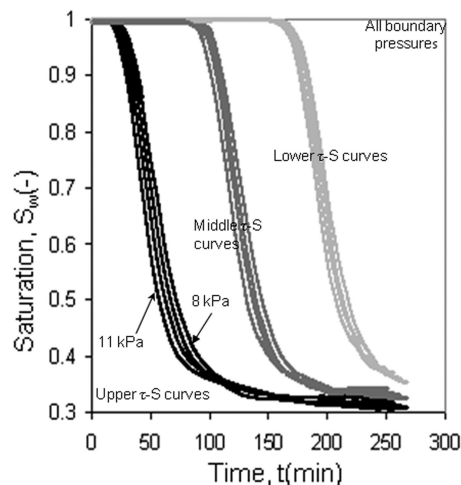
Results and Discussions

### Experimental results

Pressure Distribution in Porous Samples. In this section, we briefly discuss the distribution of pressure of the wetting and nonwetting phases in the porous samples. Figure 2 shows the boundary and the local fluid pressures at three different heights within the sample measured by selective PTs. The figure shows that a pair of PTs mounted at the same height show similar behavior before an advancing front of silicone oil reaches them. As soon as the silicone oil reaches the hydrophobic filter in an oil PT, it shows an increase in pressure. This is because of the hydrophobicity of the filter which allows only the oil to flow through the filter and reaches the oil in the oil compartment that exists in front of the PT. However, the water PT reads a constant pressure since the oil cannot flow through hydrophilic filter but still insert hydrostatic head on the filter. The differences in the pressures of the nonwetting and wetting phases at a certain height in the domain are determined, which are the capillary pressures (P^c) at that height in the domain. These P^c data are then used to construct the P^c-S_w curves. The results presented in Figure 2 are only for the case when the pressure of the nonwetting phase is 8 kPa on the sample boundary. Similar trends are found for the other values of boundary pressures and are not included in this article.

Water Saturation (S_w) Distribution in Porous Sample. Figure 3 shows the changes of water saturation (S_w) with time at three

Figure 2. Pressure transducers readings for boundary pressure (oil pressure) of 8 kPa applied on the top boundary in coarse sand domain.

Figure 3. Saturation vs. time (S_w-t) in coarse sand for boundary oil pressures of 8, 9, 10, and 11 kPa.
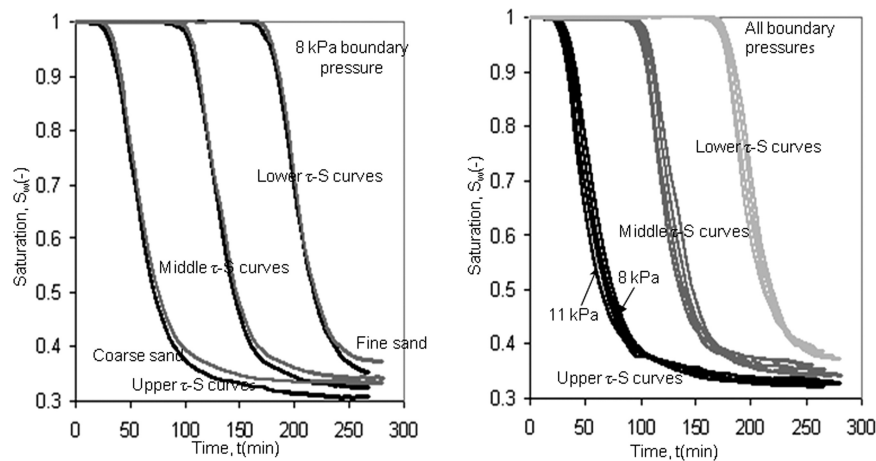
Figure 4. (a) S_w-t curves in fine and coarse sand domains for 8 kPa boundary pressure; (b) S_w-t curves of fine sand domain for all boundary conditions in dynamic flow condition.

different heights within the porous domain as the silicone oil displaces water out of the cell containing coarse sand. In the figure S_w values at different heights of coarse sand are plotted against the time elapsed from the beginning of the experiments. The oil pressures at the domain boundary are indicated in the figures. As evident in the figure the TDR probe shows slightly higher irreducible water saturation (S_{rw}) at the middle of the domain in comparison to that of the upper probe. In contrast, the lowest probe shows that S_{rw} at the bottom of the domain is higher as compared to the upper and middle parts of the domain. This is somewhat expected as our experimental rig mimics that of a pressure cell. Consequently when the front of the silicone oil reaches the lower hydrophilic filter in our experimental cell, it cannot flow any further and it tends to accumulate over the filter. This prevents smooth outflow of water near the bottom of the cell and results in higher S_{rw} at the bottom of the porous sample. The bypassed and isolated water in the porous sample cannot be mobilized which seems to result in a stabilized S_w-t profile in the middle and especially the lower part of the domain. If the saturation–time (S_w-t) curves are superimposed for a certain boundary condition they would show that although the probes in different heights do not result in similar residual saturation values the curves have very similar profiles. Figure 3 also shows the S_w-t curves at the three different heights for all dynamic flow conditions in one figure. As expected, the figure shows that the higher is the boundary pressure, the higher is the residual saturation. In higher boundary pressure, the advancing front reaches the probes earlier compared to a lower boundary pressure. The S_w-t curves show very consistent trend in all locations.

Figure 4a displays a comparison between S_w-t curves for the fine and coarse sand at different heights in the samples for silicone oil pressure of 8 kPa. As expected, the advancing nonwetting phase takes longer to reach the upper measurement height in the fine sand domain than in coarse sand domain due to the lower permeability of the fine sand. The figure also shows that the residual water saturations are higher in the fine sand domain due to smaller pore size and consequently lower permeability of fine sand domain. Similar trends are observed for the other oil boundary pressures, i.e., 9, 10, and 11 kPa.

The figures show that the S_w is higher in fine sand than that in the coarse sand at the same time. Also, for different

boundary conditions, the residual water saturation is higher towards the bottom of the domain in both the media although this is more pronounced in fine sand. Residual water saturation increases with increasing boundary pressure. It is obvious, therefore, both the boundary conditions and porous media types affect the distribution and value of S_{rw}. Figure 4b shows that similar to the coarse sand domain, higher boundary pressure results in faster displacement of water by the nonwetting phase in fine sand. It implies that at higher boundary pressure (11 kPa oil pressure in this case) an advancing oil front reaches a measurement point earlier than the lower boundary pressure displacement (8 kPa oil pressure in this case), which is consistent with the expected results.

Quasi-Static P^c-S_w Relationships in Porous Samples. Quasi-static P^c-S_w curves have been discussed extensively in the literature and are well understood. However, we present some typical results of our experiments for the completion of the discussions and since these curves are needed for determining the dynamic coefficients. Figure 5 displays the quasi-static P^c-S_w curves for drainage of coarse and fine sand domains. The P^c-S_w curves are determined from both the local and boundary capillary pressure data. As expected and shown in Figure 5a for coarse sand domain, the P^c-S_w curves calculated from the local pressure and water saturation measurements overlay the P^c-S_w curves calculated from the boundary pressures and cumulative water drained out of sample. This is because at quasi-static conditions, the local P^c-S_w curves follow the P^c-S_w curves measured from the boundary P^c data. For simplicity, we will call the P^c-S_w curves measured from the boundary data as effective quasi-static P^c-S_w curve from now on. Also, a comparison of P^c-S_w curve determined for drainage of fine and coarse sand domains (Figure 5b) shows that the P^c-S_w curves for the porous medium with lower intrinsic permeability (fine sand in this case) lies higher which is consistent with the expected trend.

To verify the reliability of the experimental data, experiments with oil pressure of 10 kPa at the top boundary of the domains were also conducted to obtain quasi static P^c-S_w curves. It was found that the results of the original and repeated experiments almost overlapped. This gave the confidence that the experiments have been conducted correctly and the results can be reproduced using the developed experimental rig.
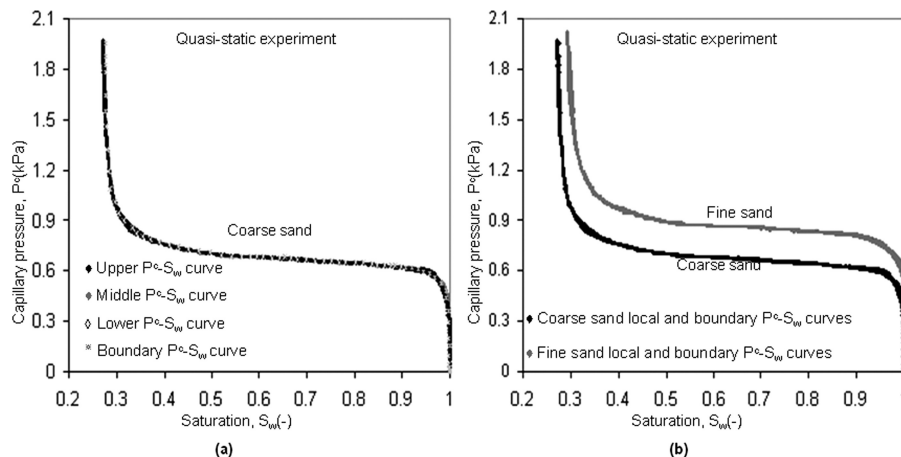
Figure 5. Quasi-static capillary pressure curves (a) coarse sand quasi-static P^c-S_w curves determined from locally measured and boundary pressure and saturation data and (b) effective quasi-static P^c-S_w curves determined from local and boundary data for coarse and fine sands.

Dynamic P^c-S_w Relationships in Porous Samples In this section, we discuss some typical results for the dynamic P^c-S_w relationships. These experimental results include the dynamic P^c-S_w curves determined from locally measured phase pressures and saturation at different locations for different boundary conditions for coarse and fine sand domains. The P^c-S_w curves at different locations follow similar trends and almost overlay in both coarse and fine sand domains. This consistent behavior is shown irrespective of the boundary conditions. However, at higher boundary pressure (11 kPa, for instance) the local capillary pressure at the lowest measurements location shows slightly different behavior towards the lower saturation. In both the fine and coarse sand domains, the higher boundary pressures result in higher residual saturation. This is expected as shown in S_w-t profiles in both fine and coarse sand domains. Figure 6 displays a comparison of the local dynamic P^c-S_w curves in coarse and fine sand domains. Similar to the quasi-static flow conditions, the local dynamic P^c-S_w curves in the fine sand domain lie higher. Figure 6 also demonstrates that the dynamic P^c-S_w curves depend on the applied boundary pressure and
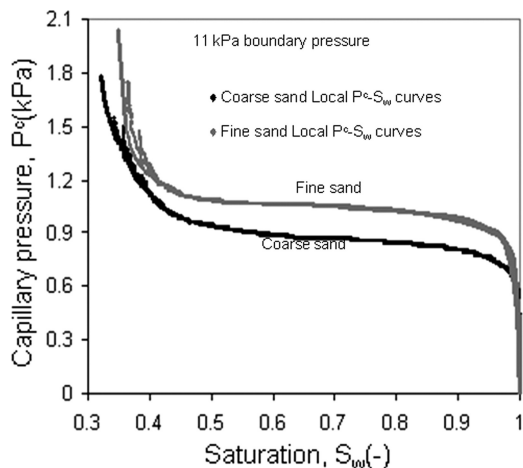
Figure 6. Comparison of dynamic P^c-S_w curves at boundary pressures of 11 kPa for fine and coarse sands.

Similar trends are observed for boundary pressures of 8, 9, and 10 kPa.

porous media properties such as the permeability and pore size distribution. Furthermore, for porous media with the same properties, there is not a unique P^c-S_w curve.

Calculation of Dynamic Coefficient (τ). Equation 2 shows that if P^{c,dyn}-P^{c,equ} and $\partial S_w/\partial t$ are known at a given saturation value, τ can be determined. Having determined the P^{c,equ} and P^{c,dyn} in both fine and coarse sand domains, we plot the curves at the same measurement heights for calculating the dynamic coefficient. For example, Figure 7 shows a set of typical quasi-static and dynamic P^c-S_w curves at the middle of the fine and coarse sand domains which are used for calculating the dynamic coefficient at this location. The higher the boundary pressure, the further away from the quasi-static curve the dynamic curves lie, for both media types. Similar, trends are observed at other locations in the domain.

$\partial S_w/\partial t$–t Relationships at Different Heights of Porous Sample. In this section, we discuss the time derivative of saturation ($\partial S_w/\partial t$) vs. time (t) curves for fine and coarse sand domains. $\partial S_w/\partial t$ is the slope of a S_w-t curve, and hence the rate of change of saturation at a particular time. In our case, the $\partial S_w/\partial t$-t relationships indicate how the rates of change of saturation may vary with time as the silicone oil displaces water out of the cell which in turn determines the dynamic coefficient (see Eq. 2). As expected, $\partial S_w/\partial t$ is not constant and varies with time. Figure 8 displays the $\partial S_w/\partial t$-t determined from the locally measured saturations at different locations in fine and coarse sand domains. The Figures 8a–c use the time elapsed from the start of the experiment while Figure 8d uses the time from the moment of first change of saturation occurs. As shown in this figure, fine sand domain results in slightly higher $\partial S_w/\partial t$ values compared to coarse sand domain. Superimposed $\partial S_w/\partial t$–t curves (Figure 8d) for fine and coarse sand domains are also compared which again show the consistency in the behavior of curves. Also, $\frac{\partial S_w}{\partial t}$–t relationships determined at the three different heights of coarse sand domain show that there is a slight discrepancy in the lower measurement point where the higher residual saturation may be high at higher boundary pressure. The curves in Figures 7 and 8 are used to find P^{c,dyn}-P^{c,equ} and $\partial S_w/\partial t$–t for the calculation of local τ-S_w relationships.

τ-S_w Relationships at Different Heights of Porous Sample. In this section, we discuss how the dynamic coefficients are calculated. For this purpose, the values of P^{c,dyn}-
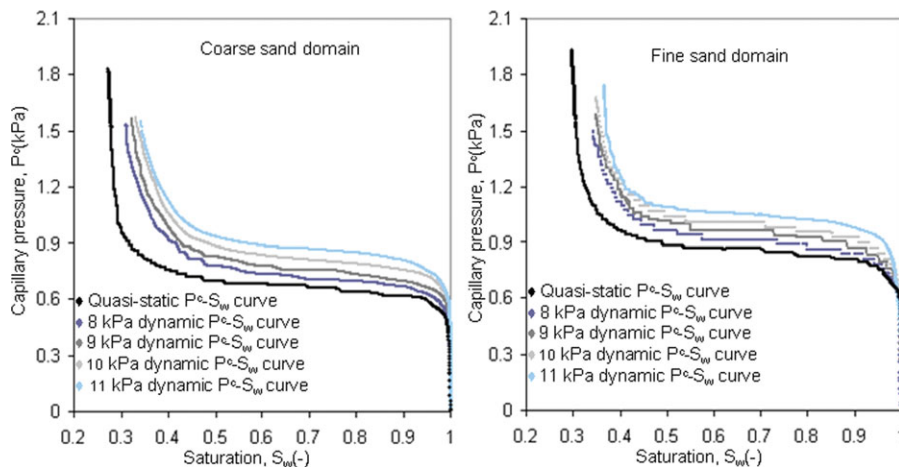
Figure 7. (a, b) Local dynamic and quasi-static P^c-S_w curves at the middle measurement height of coarse and fine sand domains.

Similar trends are observed at the upper and lower measurement points. [Color figure can be viewed in the online issue, which is available at wileyonlinelibrary.com.]

$P^{c,equ}$ and $\partial S_w/\partial t$ at various saturation are determined as presented in Figures 7 and 8 at three different heights in the fine and coarse sand domains. A plot of $P^{c,dyn}$-$P^{c,equ}$ v/s $\partial S_w/\partial t$ is necessary to calculate τ. A typical plot at the middle of the coarse sand domain is presented in Figure 9. As shown in this figure, straight lines can be fitted to the data points at different saturation values. Based on Eq. 2, the slope of these straight lines is defined as τ for that particular saturation value.

Figure 10 shows the results for locally calculated τ-S_w curves for drainage of fine and coarse sand domains. Figure 10a shows τ-S_w dependence at the upper measurement point of coarse and fine sand domains. Highlighted part of the graph is magnified in Figure 10b for $0.5 < S_w < 1$ to show the difference in dynamic coefficient and its values at higher saturation for both porous medium types. Although in Figure 10a the dynamic coefficient seems to be small and remains fairly constant for coarse sand domain in higher saturation
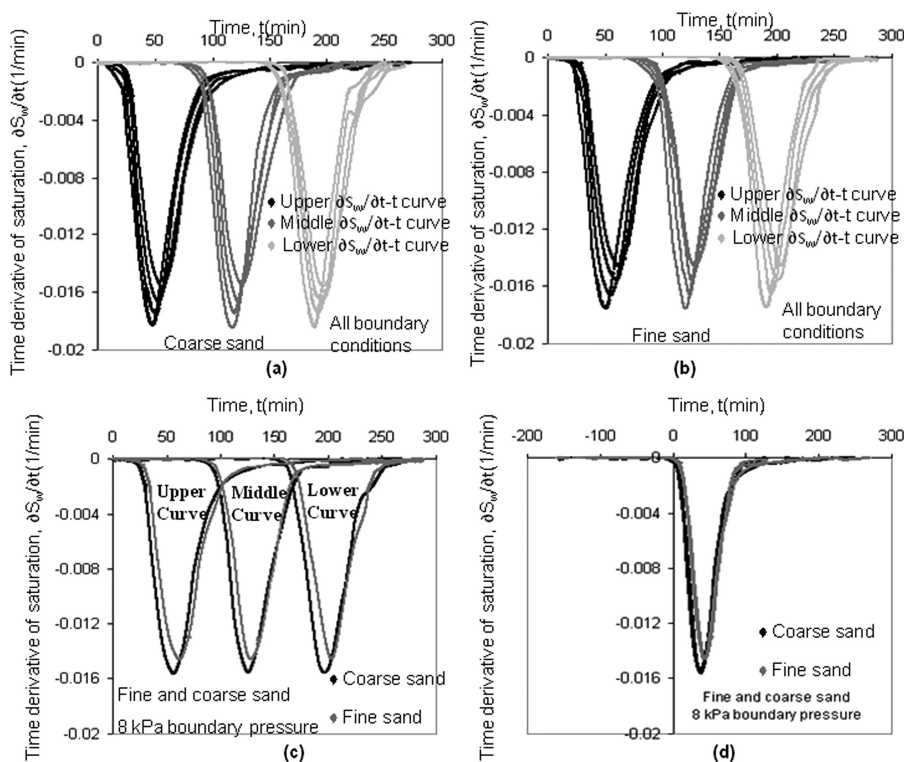
Figure 8. (a, b) $\partial S/\partial t$-t curves in coarse and fine sand domain for all boundary conditions; (c, d) $\partial S/\partial t$-t curves in fine and coarse sand domains for 8 kPa boundary pressure.

Similar comparisons of the curves are observed for other boundary conditions. The Figures 8a–c use the time elapsed from the start of the experiment while Figure 8d uses the time from the moment of first change of saturation occurs.
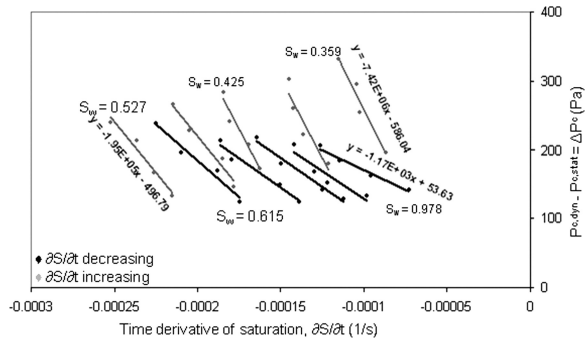
Figure 9. Plot of the difference between dynamic and quasi-static P^c-S_w curve ($P^{c,dyn}$ –$P^{c,stat}$ = ΔP^c) vs. time derivative of saturation ($\partial S_w/\partial t$) for dynamic coefficient (τ) calculation at the middle measurement point of coarse sand domain.

range, Figure 10b shows that this may not be the case. Figures 10c, d show the τ-$S_w$curves at the middle and lower measurement heights of both sands. As evident, the dynamic coefficient increases as saturation decreases at all measurement heights but this is not a linear dependence. Also, the dynamic coefficient is higher in the fine sand domain at the same saturation in all heights.

In terms of relaxation time and/or required force/energy to reach quasi-static condition, the local τ-$S_w$data in Figures 10a–d show that within a homogeneous domain of particular physical properties such as permeability, porosity and pore

size distribution, the required energy/relaxation time to force the equilibrium may not depend on the location of measurement point within the domain. However, they strongly depend on the saturation of wetting phase. The results show that the system at lower water saturation needs much higher dynamic coefficient to reach the quasi-static condition, implying the dependence of the coefficient on porous media properties.

Effective τ-S_w Relationships. Because the τ-$S_w$curves follow fairly consistent trend in different locations in both fine and coarse sand domains, one could average the data and present an effective t-$S_w$curves as a function of average water saturation for the whole domain, as shown in Figure 11. The average values are calculated by using the following equations

$$\langle S_w \rangle = \frac{\sum_{i=1}^{i=n} \left(S_w \Big|_{t_n \cdot} \right)_{V_i} V_i}{\sum_{i=1}^{i=n} V_i} \quad (9)$$

$$\langle \tau \rangle \Big|_{\langle S \rangle} \cdot = \frac{\sum_{i=1}^{i=n} \left(\tau \times S_w \Big|_{t_n \cdot} \right)_{V_i} V_i}{\sum_{i=1}^{i=n} \left(S_w \Big|_{t_n \cdot} \right)_{V_i} V_i} \Big|_{\langle S \rangle} \cdot \quad (10)$$

where $\langle S_w \rangle$ is volume weighted water saturation which is also the average/effective water saturation, $\langle \tau \rangle|_S$ is saturation weighted dynamic coefficient (τ), which is the average/effective τ and presented as a function of average/effective
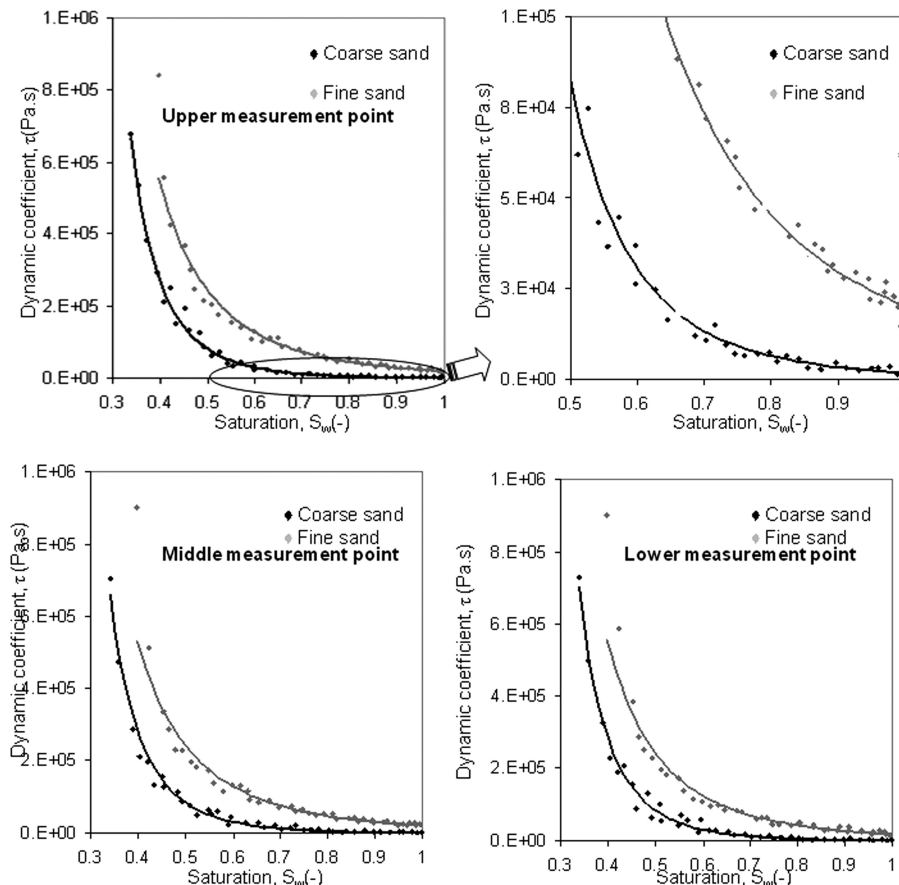
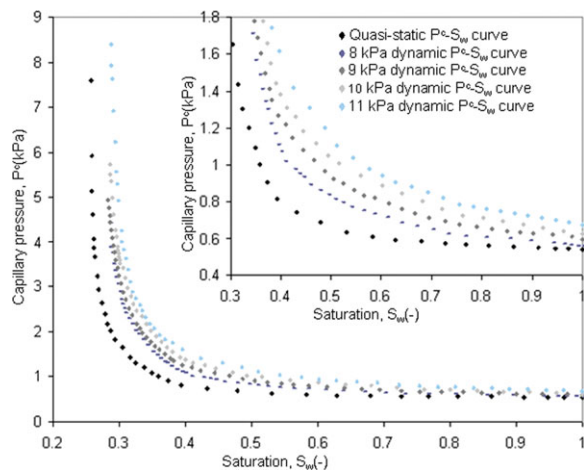**Figure 10. (a–d). Dynamic coefficient vs. saturation data in fine and coarse sand domains.**
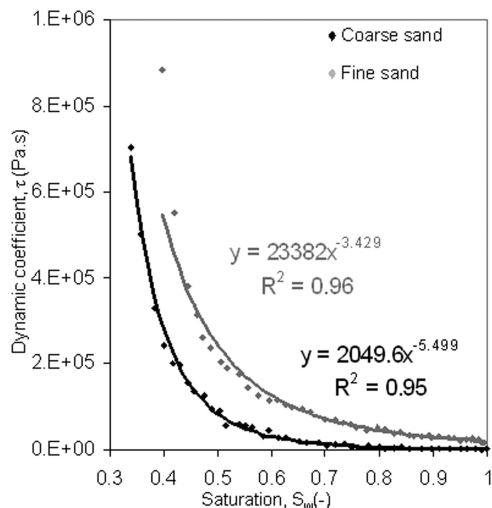
Figure 11. Average dynamic coefficient vs. saturation relationships for fine and coarse sand domains.

Figure 13. Numerical τ-S_w data calculated at the upper, middle and lower measurement volumes and effective τ-S_w data (the line).

[Color figure can be viewed in the online issue, which is available at wileyonlinelibrary.com.]

saturation. $(\tau)_{V_i}$ is the dynamic coefficient and $(S_w|_{t_n})_{V_i}$ is the measured saturation at measurement volume V_i at corresponding measurement height i, and $i = 1,2,3,\ldots,n$ is the number of measurements heights in which the τ-S_w curves are calculated, i.e., the number of τ-S_w curves, in which $n = 3$.
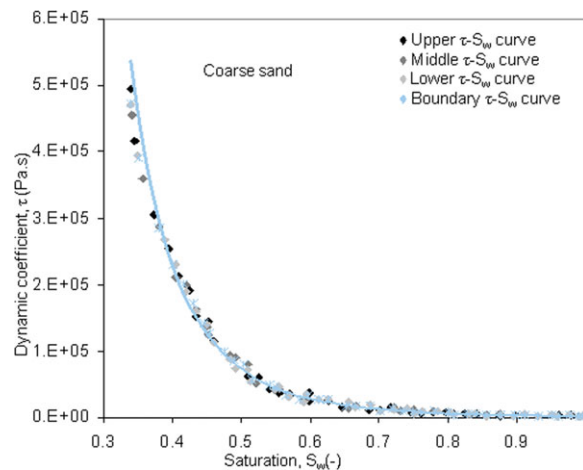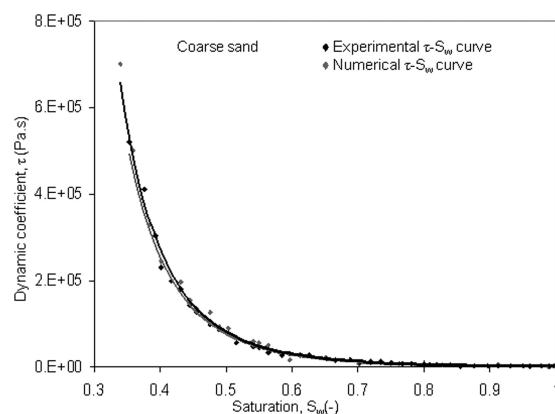
Figure 11 presents the average τ-S_w curves in coarse and fine sand domains. Again, the τ-S_w curves in the fine sand domain lie above that for coarse sand domain. This means that the fine sand domain requires more force to reach quasi-static flow condition.

Having found the τ-S_w relationships at different heights of sample, one may use different averaging methods (volume weighted average as is used in this research, arithmetic average, geometric average, harmonic average, etc.) to find an average value for the whole domain. In this study, saturation weighted averaging of three locally measured τ-S_w curves (Eq. 10) is used. The patterns of the curves are similar to the ones observed previously by many authors.

Numerical analyses

In an attempt to simulate the dynamic and quasi-static two-phase flow in homogeneous domains, corresponding P^c-S_w curves at three measurement volumes are determined. Figure 12 displays the results of the dynamic and quasi-static numerical experiments for the middle measurement volume of numerical coarse sand domain. Similar to laboratory experiments, the averaged dynamic P^c-S_w curves lie higher than the averaged quasi-static P^c-S_w curves. In the numerical experiments, the practical problems such as breakthrough of nonwetting phase through lower filter do not happen. Therefore, the displacement continues until the residual water saturation distribution is similar throughout the domain. At this condition, the range of capillary pressure is also higher (Figure 12). Therefore, the capillary pressure–saturation curves for lower capillary pressure values (or higher saturation values) are suppressed and P^c-S_w trends are not clear. To show P^c-S_w curves for lower capillary pressure values, the P^c-S_w curves are magnified for $0.4 < P^c < 1.8$ kPa. As shown in Figure 12, the higher boundary pressure results in higher capillary pressure in the beginning of numerical experiment, when average saturation is high. This is logical considering the fact that the Brookes-Corey-Burdine formulations[20] are

Figure 12. Average/effective dynamic and quasi-static P^c-S_w curves at the middle measurement volume of a coarse sand domain.

[Color figure can be viewed in the online issue, which is available at wileyonlinelibrary.com.]

Figure 14. Comparison of experimental and numerical effective τ-S_w relationships for coarse sand.

used in numerical model to perform modeling of fluid flow in porous media. The same trend is observed at upper and lower measurement volumes.

The same procedure explained earlier is used to calculate the dynamic coefficient at three measurement volumes in the numerical domain. Figure 13 shows three τ-S_w data sets calculated at different measurement volumes and effective τ-S_w data calculated using Eqs. 9 and 10. As is shown in this figure, the local τ-S_w data follow consistent trend and overlie. Effective τ-S_w data align with the local τ-S_w data. As shown in the experimental results, the dynamic coefficient is a nonlinear function of water saturation and increases as water saturation decreases. Figure 14 shows a comparison of the average τ-S_w data calculated from numerical and laboratory experiments performed on a coarse sand domain. As evident from the figure, the experimental and numerical effective τ-S_w data overlie. It is clear that the results of the experiments may be predicted using the numerical models presented earlier.[2,3,4]

Conclusions

The article is aimed at direct experimental determination of dynamic and quasi-static capillary pressure-saturation curves for two-phase flow in homogeneous porous medium three-dimensional (3D). Experimental techniques have been designed to accommodate PTs and TDR probes within 3-D porous materials of high permeability for in situ measurements of phase pressures and water saturation. Measurements are generally conducted under specified boundary conditions over reasonable time periods. The major advantage of this approach lies in the possibility of gathering the necessary information to describe two-phase flow behavior at dynamic and equilibrium conditions for drainage displacement for the sample material.

In this article, we have presented our experimental study for two-phase flow in 3-D cylindrical domains for flow in vertical direction along gravity. The postbreakthrough transient responses of the total wetting phase saturation and pressure drop across the porous medium are measured. The measured dynamic P^c-S_w curves are compared to the corresponding steady-state results and potential differences are interpreted in the light of the mechanisms governing the dynamic two-phase flow in porous media. Our results clearly confirms that the P^c-S_w relationships are not unique and depend on the flow dynamics, i.e., steady state or dynamic and the permeability of porous, among other factors. This is in consistent with our previous numerical results.[2,3,25] Our also results show that the linear relationship proposed in literature for dynamic capillary pressure is generally valid. In drainage of porous media, the dynamic coefficient is a nonlinear function of water saturation which increases as saturation decreases. In other words, the flow system needs higher amount of energy to reach equilibrium as saturation decreases. Also, saturation weighted average of τ-S_w relationships calculated at different locations of a domain gives an indication of effective τ-S_w curves for a domain.

The method adopted in this work has the advantage of directly measuring the pressure of the wetting and nonwetting phases and saturation profiles within the sample, which enable a simultaneous determination of local capillary pressure and consequently local dynamic coefficient. However, (1) minimizing uncertainty on the distribution of fluids near the effluent, the way in which the end effects are reduced

and (2) the effect of heterogeneities on τ-S_w relationship will be explored in future.

Simulation carried out in this work show that τ-S_w relationships can be predicted using previously developed numerical schemes[2,3,4].

Literature Cited

1. Mirzaei M, Das DB, Sills GC. Dynamic effects in capillary pressure-saturation relationship for two-phase flow in porous media: experiments and numerical simulations. In: Proceeding of the ITP2007 Interdisciplinary Transport Phenomena V: Fluid, Thermal, Biological, Materials and Space Sciences, October 14–19, Bansko, Bulgaria, 2007.
2. Mirzaei M, Das DB. Dynamic effects in capillary pressure-saturations relationships for two-phase flow in 3d porous media: implications of micro-heterogeneities. *Chem Eng Sci.* 2007;62:1927–1947.
3. Das DB, Gauldie R, Mirzaei M. Dynamic effects for two-phase flow in porous media: fluid property effects. *AIChE J.* 2007;53:2505–2520.
4. Hanspal N, Das DB. Dynamic effects on capillary pressure-saturation relationships for two-phase porous flow: implications of temperature. *AIChE J.* 2012, DOI: 10.1002/aic.12702.
5. Kalaydjian F. Dynamic capillary pressure curve for water/oil displacement in porous media: theory vs. experiment. Presented at the SPE Conference, Washington, DC, SPE24813, October 4–7, 1992.
6. Hassanizadeh SM, Gray WG. Thermodynamic basis of capillary pressure in porous media. *Water Resources Res.* 1993;29:3389–3405.
7. Beliaev AY, Hassanizadeh SM. A theoretical model of hysteresis and dynamic effects in the capillary relation for two-phase flow in porous media. *Transport Porous Media.* 2001;43:487–510.
8. Beliaev AY, Schotting RJ. Analysis of a new model for unsaturated flow in porous media including hysteresis and dynamic effects. *Comput Geosci.* 2001;222:345–368.
9. Hassanizadeh SM, Celia MA, Dahle HK. Dynamic effect in the capillary pressure-saturation and its impact on unsaturated flow. *Vadose Zone J.* 2002;1:38–57.
10. Barenblatt GJ, Patzek TW, Silin DB. The mathematical model of non-equilibrium effects in water-oil displacement. *Soc Pet Eng.* 2003;84:409–416.
11. Dahle HK, Celia MA, Hassanizadeh SM. Bundle-of-tubes model for calculating dynamic effects in the capillary pressure-saturation relationship. *Transport Porous Media.* 2005;58:5–22.
12. O'Carroll DM, Phelan TJ, Abriola LM. Exploring dynamic effects in capillary pressure in multistep outflow experiments. *Water Resour Res.* 2005;41:W11419.
13. Oung O, Hassanizadeh SM, Bezuijen A. Two-phase flow experiments in a geocentrifuge and the significance of dynamic capillary pressure effect. *Porous Media* 2005;8:247–257.
14. Oung O, Schenkeveld FM, Weststrate F. Centrifuge research on the transport of DNAPLs: the use of dielectric water content sensors to study DNAPL transport into porous media in centrifuge experiments. In: Proceedings of the International Symposium on Physical Modelling and Testing in Environmental Geotechnics, La Baule, May 15–17, 2000:317–324. ISBN 2-7208-6050-6.
15. Manthey S, Hassanizadeh SM, Helmig R. Macro-scale dynamic effects in homogeneous and heterogeneous porous media, *Transport Porous Media.* 2005;58:121–145.
16. Bottero S, Hassanizadeh SM, Kleingeld PJ, Bezuijen A. Experimental study of dynamic capillary pressure effect in two-phase flow in porous media. In: Proceedings of the XVI International Conference on Computational Methods in Water Resources (CMWR), Copenhagen, Denmark, 18–22 June, 2006.
17. Gielen TWJ. Dynamic effects in two-phase flow in porous media: a pre scale network approach. PhD thesis, Delft University of Technology, Delft, The Netherlands, 2007.
18. O'Carroll DM, Mumford KG, Abriola LM, Gerhard JI. Influence of wettability variations on dynamic effects in capillary pressure. *Water Resour Res.* 2010;46:10.1029/2009WR008712.

19. Joekar-Niasar V, Hassanizadeh SM, Dahle HK. Non-equilibrium effects in capillarity and interfacial area in two-phase flow: dynamic pore-network modeling. *J Fluid Mech*. 2010;655:38–71.
20. Sakaki T, O'Carroll DM, Illangasekare TH. Direct quantification of dynamic effects in capillary pressure for drainage-wetting cycles. *Vadose Zone J*. 2010;9:424–437.
21. Fucik R, Mikyska J, Sakaki T, Benes M, Illangasekare TH. Significance of dynamic effect in capillarity during drainage experiments in layered porous media. *Vadose Zone J*. 2010;9:697–708.
22. Peszynska M, Yi SY. Numerical methods for unsaturated flow with dynamic capillary pressure in heterogeneous porous media. *Int J Num Anal Model*. 2008;5:126–149.
23. Brooks RH, Corey AT. *Hydraulic Properties of Porous Media. Hydrology Papers*. Colorado State University, 1964.
24. Adamson AW, Gast AP. *Physical Chemistry of Surfaces*, 6th ed. Wiley-Interscience, 1997:784. ISBN 0-471-14873-3.
25. Das DB, Mirzaei M, Widdows N. Non-uniqueness in capillary pressure—saturation—relative permeability relationships for two-phase flow in porous media: implications of intensity and random distribution of micro-heterogeneity. *Chem Eng Sci*. 2006;61:6786–6803.